nature energy

SUPPLEMENTARY INFORMATION

https://doi.org/10.1038/s41560-019-0535-7

In the format provided by the authors and unedited.

Ligand-assisted cation-exchange engineering for high-efficiency colloidal $Cs_{1-x}FA_xPbI_3$ quantum dot solar cells with reduced phase segregation

Mengmeng Hao[1], Yang Bai[1*], Stefan Zeiske[2], Long Ren[3], Junxian Liu[4], Yongbo Yuan[5], Nasim Zarrabi[2], Ningyan Cheng[3], Mehri Ghasemi[1], Peng Chen[1], Miaoqiang Lyu[1], Dongxu He[1], Jung-Ho Yun[1], Yi Du[3], Yun Wang[4], Shanshan Ding[1], Ardalan Armin[2], Paul Meredith[2], Gang Liu[6,7], Hui-Ming Cheng[6,8,9] and Lianzhou Wang[1*]

[1]Nanomaterials Centre, Australian Institute for Bioengineering and Nanotechnology and School of Chemical Engineering, The University of Queensland, St Lucia, Queensland, Australia. [2]Department of Physics, Swansea University, Swansea, UK. [3]Institute for Superconducting and Electronic Materials, Australian Institute for Innovative Materials, University of Wollongong, Wollongong, New South Wales, Australia. [4]School of Environment and Science, Centre for Clean Environment and Energy, Griffith University, Gold Coast, Queensland, Australia. [5]Institute of Super-Microstructure and Ultrafast Process in Advanced Materials, School of Physics and Electronics, Central South University, Changsha, China. [6]Shenyang National Laboratory for Materials Science, Institute of Metal Research, Chinese Academy of Sciences, Shenyang, China. [7]School of Materials Science and Engineering, University of Science and Technology of China, Shenyang, China. [8]Shenzhen Geim Graphene Center, Tsinghua-Berkeley Shenzhen Institute, Tsinghua University, Shenzhen, China. [9]Advanced Technology Institute, University of Surrey, Guildford, UK. *e-mail: y.bai@uq.edu.au; l.wang@uq.edu.au

Supplementary Material for

Ligand-assisted cation exchange engineering for high-efficiency colloidal $Cs_{1-x}FA_xPbI_3$ quantum dot solar cells with reduced phase segregation

Mengmeng Hao[1], Yang Bai[1], Stefan Zeiske[2], Long Ren[3], Junxian Liu[4], Yongbo Yuan[5], Nasim Zarrabi[2], Ningyan Cheng[3], Mehri Ghasemi[1], Peng Chen[1], Miaoqiang Lyu[1], Dongxu He[1], Jung-Ho Yun[1], Yi Du[3], Yun Wang[4], Shanshan Ding[1], Ardalan Armin[2], Paul Meredith[2], Gang Liu[6,7], Hui-Ming Cheng[6,8,9], Lianzhou Wang[1]**

* Corresponding author. Emails: l.wang@uq.edu.au (L.W.); y.bai@uq.edu.au (Y.B.).

This PDF file includes:

Supplementary Note 1 to 6

Supplementary Figures 1 to 22

Supplementary Tables 1 to 4

References

Supplementary Note 1

DFT Calculation

The density functional theory (DFT) calculations were performed by using the Vienna Ab Initio Simulation Package (VASP) code based on the projector augmented wave (PAW) method in this study [1, 2]. Electron-ion interactions are described using PAW potentials, with valence configurations of $5s^2 4d^{10} 5p^6 6s^1$ for Cs (Cs_sv_GW), $6s^2 4f^{14} 5d^{10} 6p^2$ for Pb (Pb_sv_GW), $5s^2 4d^{10} 5p^5$ for I (I_sv_GW), $2s^2 2p^2$ for C (C_GW_new), $2s^2 2p^3$ for N (N_GW_new), $2s^2 2p^4$ for O (O_GW_new) and$1s^1$ for H (H_GW). The Perdew-Burke-Ernzerhof (PBE) [3], a form of the general gradient approximation (GGA), was employed for the electron-electron exchange-correlation functional. The plane-wave kinetic energy cut-off was fixed at 520 eV to expand the smooth part of wave functions. A supercell consisting of 4 $APbI_3$ units was employed in the calculations of all cubic phase of $APbI_3$. Here, A can be Cs, FA or a mixture of these two components. We partially replaced Cs with FA to model the configurations of the $Cs_{1-x}FA_xPbI_3$ perovskite with five stoichiometric ratios (x= 0, 0.25, 0.5, 0.75, and 1) (see **Fig. S1**). During the geometry optimizations, all atoms were allowed to relax until the Hellmann-Feynman forces were smaller than 0.01 eV/Å, and the convergence criterion for the electronic self-consistent loop was set to 10^{-5} eV. The Brillouin zone was sampled using Gamma-centred (4×4×8) k-point grids for all bulk $Cs_{1-x}FA_xPbI_3$ crystals.

The cation exchange energy ΔE_{ex} was calculated as following,

$$\Delta E_{ex} = E_{total} - [\,(1-x)E_{CsPbI_3} + xE_{FAPbI_3}\,] \quad (1)$$

where E_{total}, E_{CsPbI_3} and E_{FAPbI_3} are the bulk phase energies of $Cs_{1-x}FA_xPbI_3$, pure $CsPbI_3$ and $FAPbI_3$, respectively. When $\Delta E_{ex} < 0$, it means that the A-site cation exchange process is thermodynamically preferred. In addition, we calculated the defect formation energies of iodine interstitials (I_i) and lead vacancies (V_{Pb}) defects, which can be expressed as

$$\Delta E_{I_i} = E_{I_i/Cs_{1-x}FA_xPbI_3} - \left[\, E_{Cs_{1-x}FA_xPbI_3} + \frac{1}{2}E_{I_2} \,\right] \quad (2)$$

$$\Delta E_{V_{Pb}} = E_{V_{Pb}/Cs_{1-x}FA_xPbI_3} + E_{Pb} - E_{Cs_{1-x}FA_xPbI_3} \quad (3)$$

where ΔE_{I_i} and $\Delta E_{V_{Pb}}$ are the defect formation energies of I_i and V_{Pb} defects, $E_{I_i/Cs_{1-x}FA_xPbI_3}$ and $E_{V_{Pb}/Cs_{1-x}FA_xPbI_3}$ are the energies of the $Cs_{1-x}FA_xPbI_3$ structure with I_i or V_{Pb} defect, $E_{Cs_{1-x}FA_xPbI_3}$ and E_{I_2} are the energies of $Cs_{1-x}FA_xPbI_3$ perovskite and I_2 molecule, and E_{Pb} is the average energy of each Pb atom in its bulk, respectively. For the calculations on I_2 molecules, a (20 × 20 × 20) $Å^3$ unit cell and a Γ-only *k*-point grids were used.

Supplementary Note 2

The role of OA ligands

According to our hypothesis, OA plays a key role in solvating A-site cations (FA and Cs) from QD surface and reach an equilibrium in the OA-rich environment. The mobile FA-oleate and Cs-oleate would accelerate the cation-exchange reaction, whilst the possibility of defect formation is reduced with excessive OA ligands. Assuming this hypothesis is true, we should also be able to see the occurrence of cation exchange by directly adding Cs-oleate in $FAPbI_3$ QD solution or adding FA-oleate in $CsPbI_3$ QD solution.

First, we prepared colloidal $FAPbI_3$ and $CsPbI_3$ QD solutions (10 mg/mL in hexane), which were split into three vials, respectively, as shown in Supplementary Figure 3. Cs-oleate (Cs-OA) and FA-oleate (FA-OA) were synthesized by reacting Cs_2CO_3 or formamidinium acetate with oleic acid at 80 °C in vacuum condition. By adding Cs-OA in $FAPbI_3$ QD solution, the colour changed immediately from black to brown in the first 30 s. After 30min, the solution colour turned to red indicating the conversion of $FAPbI_3$ QDs to $CsPbI_3$ QDs. Similarly, adding FA-OA in $CsPbI_3$ QD solution also leaded to rapid cation exchange reaction, which resulted in conversion of $CsPbI_3$ QDs to $FAPbI_3$ QDs. Unfortunately, such a method is not suitable for the synthesis of alloy $Cs_{1-x}FA_xPbI_3$ QDs with controlled FA/Cs ratio. This is consistent with previous work[4]. To further examine the critical role of OA, we also tried caesium acetate (CsAc), caesium iodide (CsI), formamidinium acetate (FA-Ac), and formamidinium iodide (FA-I). None of them could drive the cation exchange reaction as shown in Supplementary Figure 2. This further confirms the critical role of OA in solvating A-site cations of QDs and validates the formation of mobile Cs-oleate and FA-oleate reaching an equilibrium in the colloidal solution.

Supplementary Note 3

Ligand density estimation

Ligand density was roughly estimated using the method as shown in the flowchart below:

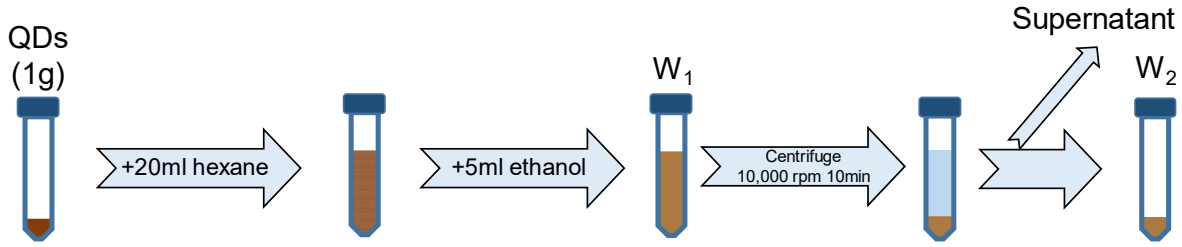

QDs with ligand are dispersed in hexane	***Ligand are stripped off without $Cs_xFA_{1-x}PbI_3$ being dissolved***	***Ligands are extracted into hexane/ethanol solution, leaving $Cs_xFA_{1-x}PbI_3$ agglomerate in the centrifuge tube***

At each stage, 1g of QDs was dried and used to determine the ligand density. Ethanol/hexane mixture was used to extract the surface ligands from the QDs. The weight of the solution was carefully determined (W_1). Then the mixture was sealed and centrifuged at 10,000 rpm for 10 mins. The supernatant (containing surface ligands, ethanol and hexane) was decanted, and the agglomerate at the bottom of centrifuge tube was dried to determine its weight (W_2). In addition, the agglomerate was used to determine the weight of lead contained in the original QDs. The amount of surface ligands was determined using the following equation: W_1-W_2-$W_{hexane/ethanol}$ ($W_{hexane/ethanol}$ is the weight of the hexane and ethanol). The ligand density at each stage was summarized in Supplementary Table 1.

Supplementary Note 4

PLQY measurement

For PLQY measurements, all the QDs were dispersed in hexane and rhodamine 6G in EtOH was used as a reference.

The PLQY can be calculated from the following equation[5]:

$$\emptyset_{\mathrm{f}}^{i}=\frac{F^{i} f_{s} n_{i}^{2}}{F^{s} f_{i} n_{s}^{2}} \emptyset_{\mathrm{f}}^{s}$$

where $\emptyset_{\mathrm{f}}^{i}$ and $\emptyset_{\mathrm{f}}^{s}$ are the photoluminescence QY of the sample and that of the standard, respectively. F^{i} and F^{s} are the integrated intensities (areas) of sample and standard spectra, respectively (in units of photons); f_x is the absorption factor (also known under the obsolete term “absorbance”), the fraction of the light impinging on the sample that is absorbed ($f_x =$

$1 - 10^{-A^x}$ where A = absorbance); the refractive indices of the sample and reference solution are n_i and n_f, respectively.

The resulting PLQYs are the average value from 5 samples in each condition.

Supplementary Note 5

STEM anlaysis

The $CsPbI_3$ QDs in Supplementary Fig. 8f show a perfect cubic perovskite structure along the [001] zone axis with Pb−I atom columns exhibiting higher contrast and Cs and I atom columns showing weaker contrast (brightened-and-dimmed contrast distributions). However, for the alloy QDs containing FA, the atomic contrast distribution in the HAADF-STEM images is different, showing some regions with uniform atomic contrast distribution instead of brightened-and-dimmed contrast distribution. The HAADF-STEM image of $FAPbI_3$ QD (Supplementary Fig. 8j) shows uniform contrast distribution for nearly all atom columns, and the atomic arrangements match very well with hexagonal PbI_2 along $[\bar{4}41]$ direction with a lattice parameter of approximately 3.2 Å[6], which we assume is due to the e-beam induced decomposition.

The atomic arrangement of $FAPbI_3$ QDs in Supplementary Figure 8j matches very well with hexagonal PbI_2 along the $[\bar{4}41]$ direction, indicating structure evolution of cubic $FAPbI_3$ QDs because of e-beam induced decomposition. Therefore, for the atomic resolution HAADF-STEM images of the samples containing both Cs and FA, the regions with uniform atomic contrast distribution can be assigned to the PbI_2 along the $[\bar{4}41]$ direction, and the other regions with brightened-and-dimmed distribution can be assigned to the $CsPbI_3$ along the [001] direction.

Supplementary Figure 9c shows the zoomed-in view of the region marked with a yellow square in experimental HAADF-STEM image (Supplementary Figure 9a) of $Cs_{0.5}FA_{0.5}PbI_3$ QD sitting in a different direction. By comparing the experimental atom arrangements with the established models, we confirmed that the atomic structure of $FAPbI_3$ along the [110] zone axis undergoes a structural evolution to PbI_2 along the $[\bar{1}\bar{1}0]$ zone axis, while the atomic structure of $CsPbI_3$ along the [110] zone was relatively stable under the e-beam irradiation.

Supplementary Note 6

Radiative and non-radiative losses

Quasi-Fermi level splitting in the bulk can be imagined as a V_{OC} in the absence of surface recombination leading to the well-known relation: $\mu_{\mathrm{bulk}} = kT\ln(\frac{Jsc}{j_0})$ derived from the Shockley equation where j_0 is the dark saturation current excluding a surface recombination contribution. Using the well-established relation between PLQY and radiative and total dark saturation current ($j_0 = j_{0,R}/\mathrm{PLQY}$) we can write $\mu_{\mathrm{bulk}} = kT\ln(\mathrm{PLQY}\frac{Jsc}{j_{0,R}})$, while the radiative limit of V_{oc} is $V_{\mathrm{oc},R} = \frac{kT}{q}\ln(\frac{Jsc}{j_{0,R}})$. $j_{0,R}$ is the radiative saturation dark current, which is calculated from integrating the product of the black body flux and external quantum efficiency measured sensitively to include the sub-bandgap states (Supplementary Fig. 20). This approach has recently been applied to perovskite thin film solar cells[41]. The non-radiative open circuit loss (excluding non-radiative surface recombination) is also determined from the PLQY so that $\Delta V_{OC,NR} = \frac{kT}{q}\ln(\mathrm{PLQY}^{-1})$. To undertake this analysis, we measured the PLQY of full devices under open circuit conditions and monochromatic (520 nm) irradiance equivalent to 1 sun. A small AC perturbation was superimposed on the pump light whose modulation was used to detect the PL signal with a high degree of sensitivity using a spectrum analyzer. The advantage of measuring PLQY of the full device under open circuit and operational illumination conditions is that the emission efficiency is measured at carrier (and indeed ion) concentrations and profiles relevant to operational open circuit. Furthermore, PLQY is related to the quasi-Fermi level splitting of the bulk, thus the results are not affected by the surface recombination.

The values of V_{OC}, μ_{bulk}, $j_{0,R}$, $\Delta V_{OC,NR}$ and $\Delta V_{OC,SR}$ for the bulk and QD devices derived from this analysis are given in Supplementary Table 4. For QD devices, PLQY values as large as 10% were obtained (at one sun-equivalent), meaning reduced non-radiative losses versus the bulk perovskite cells.

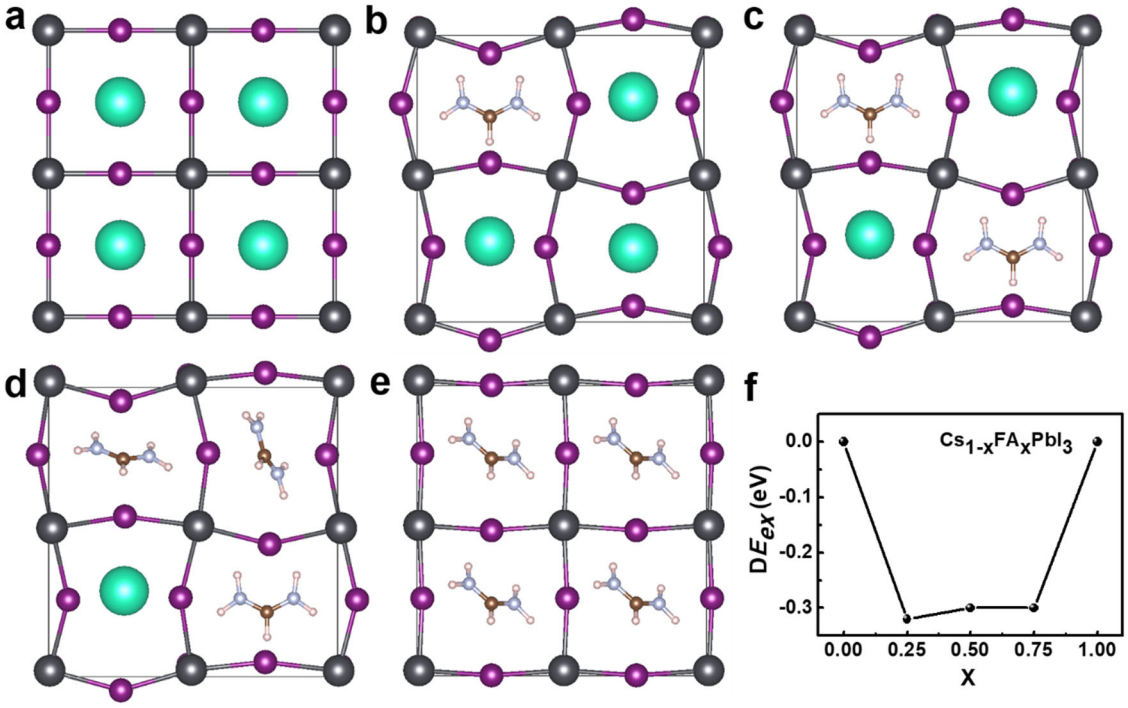

Supplementary Figure 1. Structural models of bulk $Cs_{1-x}FA_xPbI_3$ crystals. (**a**) $CsPbI_3$; (**b**) $Cs_{0.75}FA_{0.25}PbI_3$; (**c**) $Cs_{0.5}FA_{0.5}PbI_3$; (**d**) $Cs_{0.25}FA_{0.75}PbI_3$; (**e**) $FAPbI_3$. Key: Green, Cs; dark gray, Pb; purple, I; brown, C; blue, N; pink, H. (**f**) Cation exchange energy (ΔE_{ex}) required for all composition of $Cs_{1-x}FA_xPbI_3$.

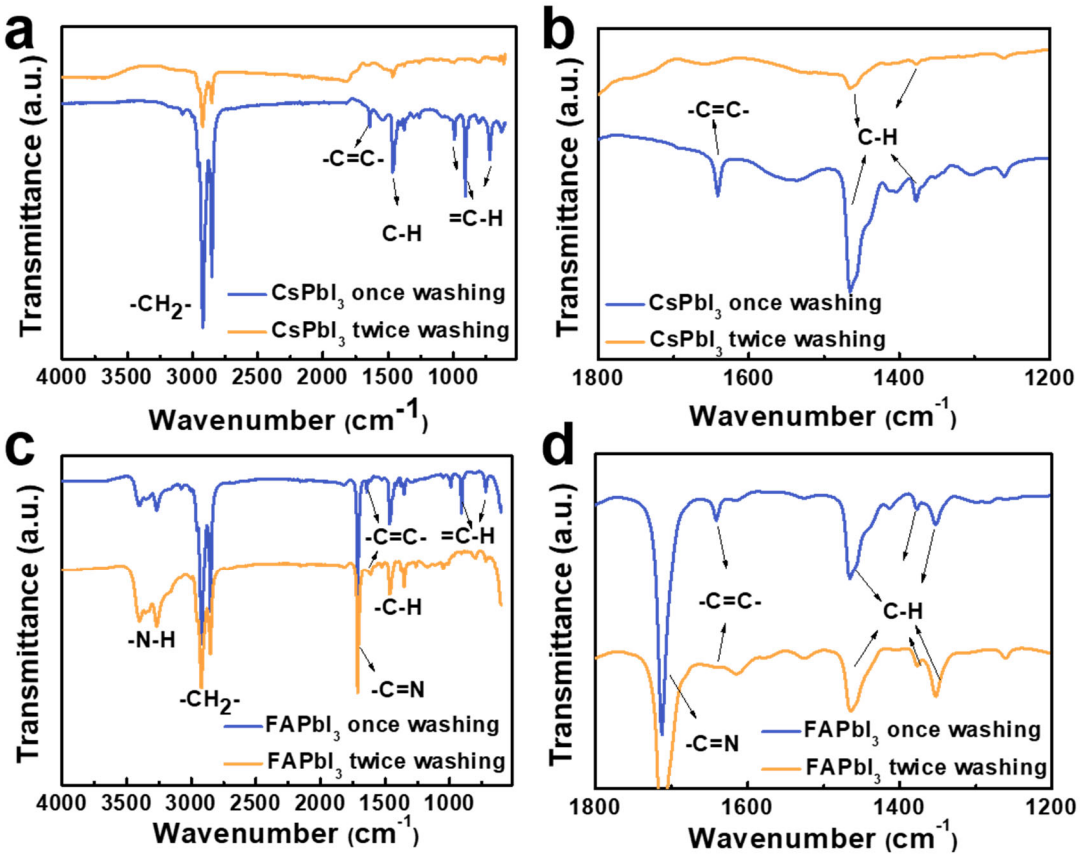

Supplementary Figure 2. Fourier-transformed infrared (FTIR) spectra of (**a**), (**b**) $CsPbI_3$ QDs and (**c**), (**d**) $FAPbI_3$ QDs. (**b**) and (**d**) are the Zoomed-in view of (**a**) and (**c**), respectively. Blue line represents QDs purified once and orange line represents QDs purified twice. The vibration bands at 1640 cm^{-1} is ascribed to –C=C– group, which is the reliable signal for monitoring the removal of OA ligands. The vibration band at 1712 cm^{-1} indexes to –C=N group, which is from FA cations. The vibration band between 2800 cm^{-1} and 3000 cm^{-1} can be indexed to $–CH_2–$ group. The vibration band between 1340 cm^{-1} and 1460 cm^{-1} is ascribed to C-H group. These two groups may come from the OA, OLA, FA or octane solvent. The vibration bands in the range of 900 cm^{-1} to 1000 cm^{-1} can be indexed to =C-H bonding, which may be from OA, OLA or FA.

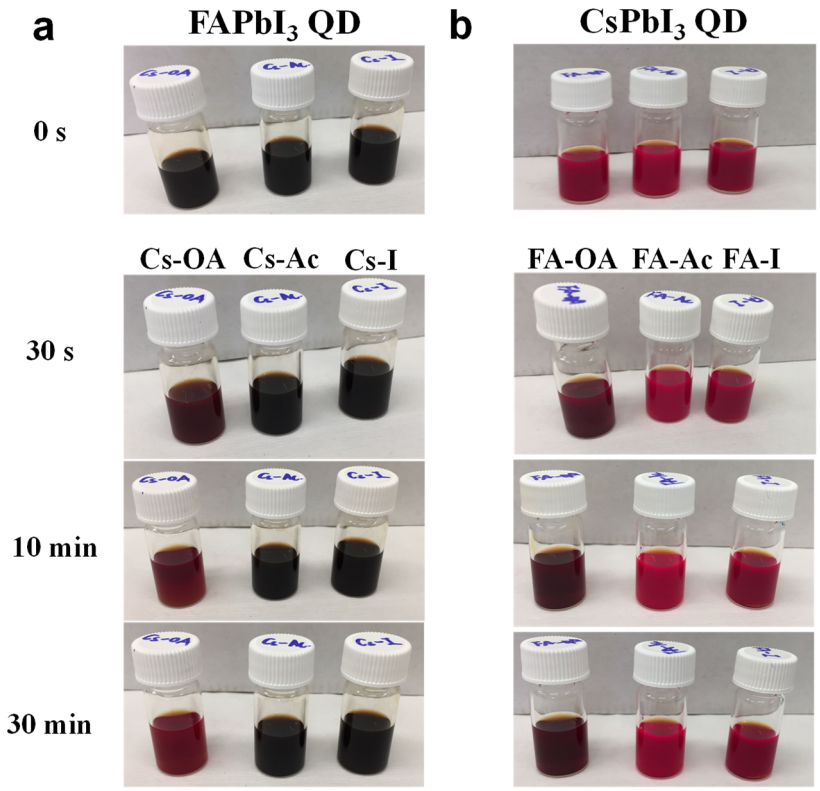

Supplementary Figure 3. (**a**) Cation exchange reaction study by adding Cs-OA, Cs-Ac, and Cs-I salts into $FAPbI_3$ QD solution. (**b**) Cation exchange reaction study by adding FA-OA, FA-Ac, and FA-I into $CsPbI_3$ QD solution. Cs-OA: Cs-oleate; Cs-Ac: Caesium acetate; Cs-I: Caesium iodide; FA-OA: FA-oleate; FA-Ac: Formamidinium acetate; FA-I: Formamidinium iodide.

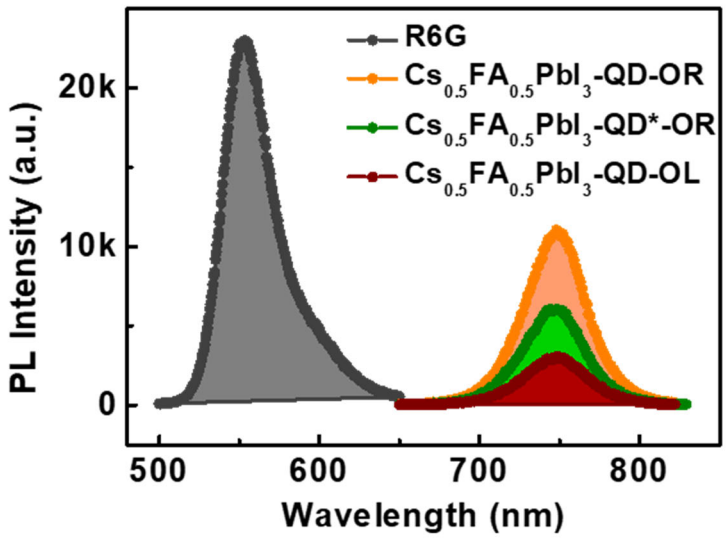

Supplementary Figure 4. PL spectra of rhodamine 6G (R6G) in ethanol (reference), as-synthesized $Cs_{0.5}FA_{0.5}PbI_3$ QDs in OA-less environment ($Cs_{0.5}FA_{0.5}PbI_3$-QD-OL), as-synthesized $Cs_{0.5}FA_{0.5}PbI_3$ QDs in OA-rich environment ($Cs_{0.5}FA_{0.5}PbI_3$-QD-OR), and $Cs_{0.5}FA_{0.5}PbI_3$-QD-OR purified once ($Cs_{0.5}FA_{0.5}PbI_3$-QD*-OR). Integrated area of different color corresponds to the PLQY of each QD sample, as they were adjusted with equal light

absorbance before PL measurements. The determined PLQY: 95% for R6G; 68% for $Cs_{0.5}FA_{0.5}PbI_3$-QD-OR; 47% for $Cs_{0.5}FA_{0.5}PbI_3$-QD*-OR; 23% for $Cs_{0.5}FA_{0.5}PbI_3$-QD-OL.

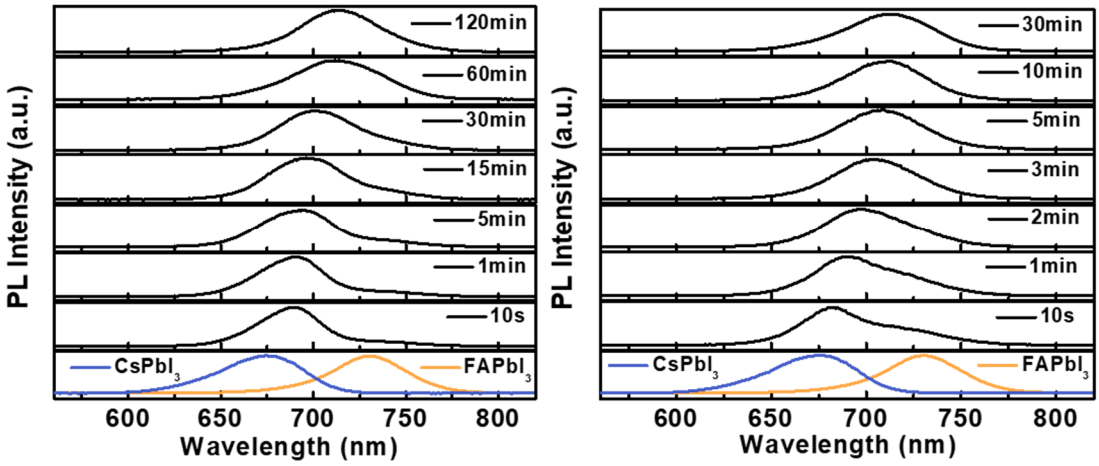

Supplementary Figure 5. The evolution of PL emission peaks with time to form $Cs_{0.5}FA_{0.5}PbI_3$ QDs by combining parent QDs in (**a**) octane and (**b**) toluene after purification for once. The bottom-most spectra in these two figures show the individual PL emissions from $CsPbI_3$ (blue) and $FAPbI_3$ (orange) QDs. The remaining emission spectra are shown for the temporal evolution with time.

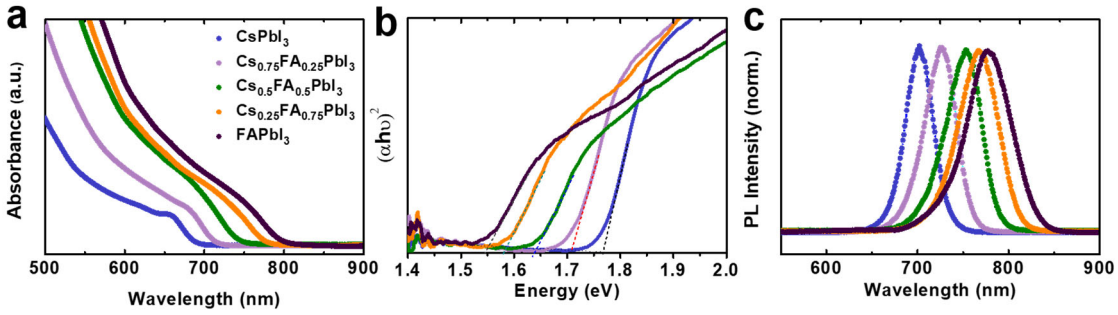

Supplementary Figure 6. (**a**) UV-vis absorption, (**b**) Tauc plots (n=1/2 for direct bandgap) and (**c**) PL emission spectra of the alloy $Cs_{1-x}FA_xPbI_3$ QDs derived in the OA-rich environment.

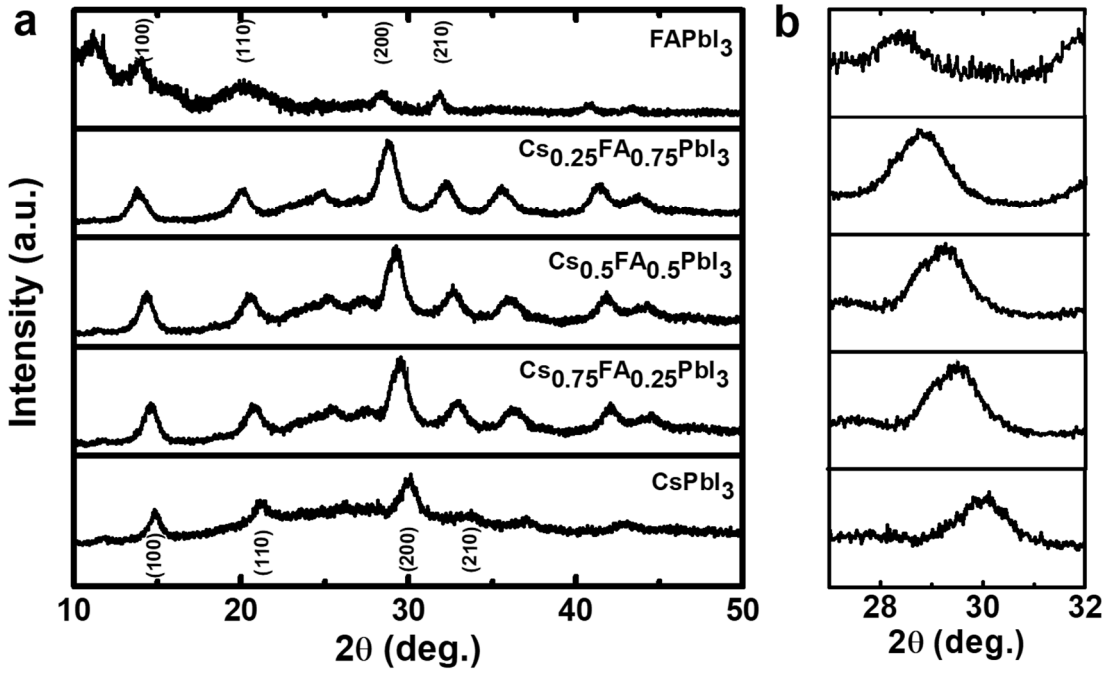

Supplementary Figure 7. (**a**) XRD patterns of $Cs_{1-x}FA_xPbI_3$ QDs. (**b**) Zoomed-in view of the (200) diffraction peak showing continuous shift from pure $FAPbI_3$ to pure $CsPbI_3$. Note that because of the relatively weaker bonding of the organic cations with inorganic cages (PbI_6 octahedra) in $FAPbI_3$ QDs compared to their inorganic counterparts, we did not perform thorough ligand treatment on $FAPbI_3$ QDs. Therefore, the noise of $FAPbI_3$ XRD data may come from the higher density of ligands on $FAPbI_3$ QD surface.

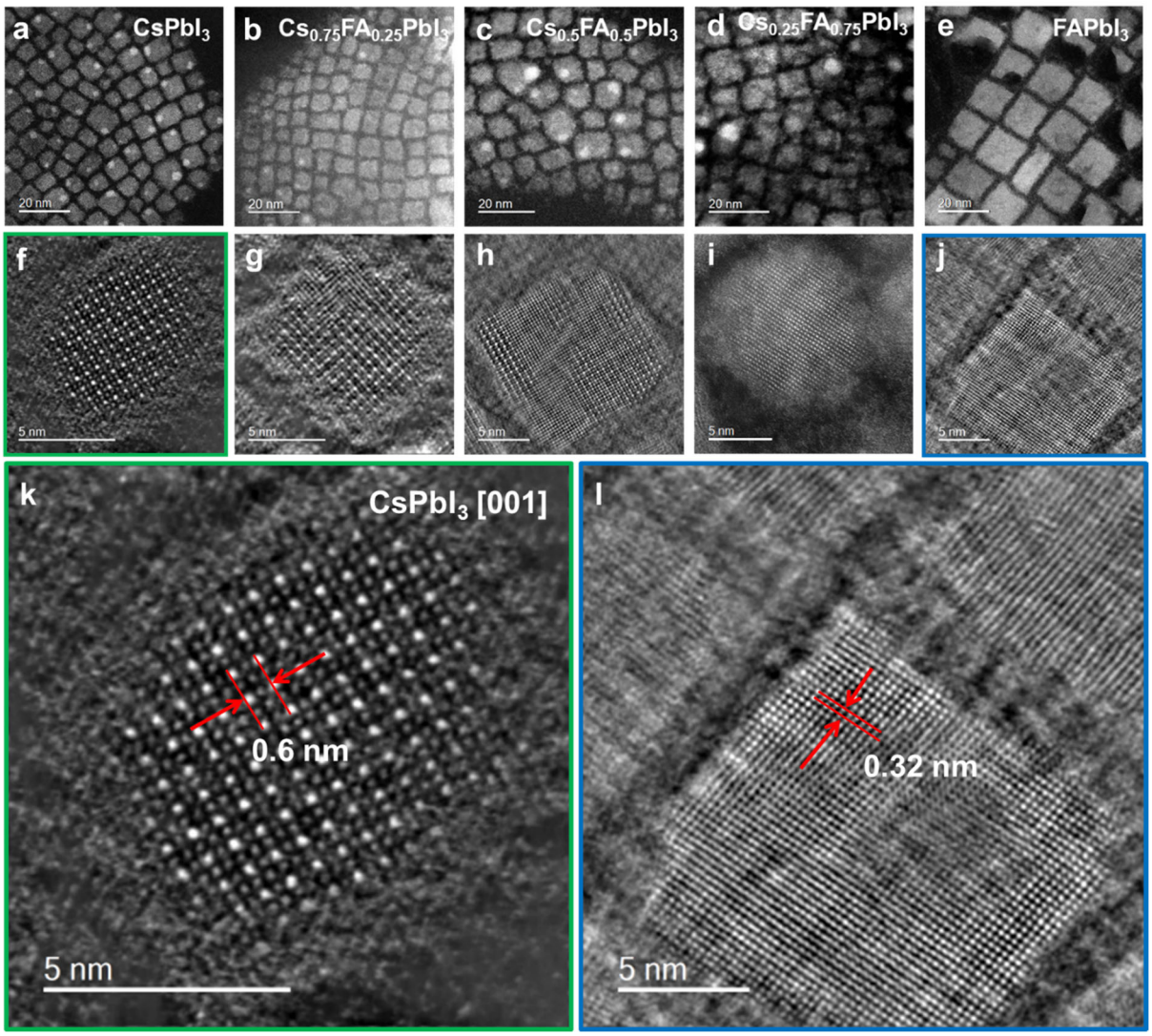

Supplementary Figure 8. HAADF-STEM images for different $Cs_{1-x}FA_xPbI_3$ samples. (**a, f**) $CsPbI_3$; (**b, g**) $Cs_{0.75}FA_{0.25}PbI_3$; (**c, h**) $Cs_{0.5}FA_{0.5}PbI_3$; (**d, i**) $Cs_{0.25}FA_{0.75}PbI_3$; (**e, j**) $FAPbI_3$; (**k**) Enlarged image of (**f**) marked with lattice parameter; (**l**) enlarged image of (**j**) marked with lattice parameter.

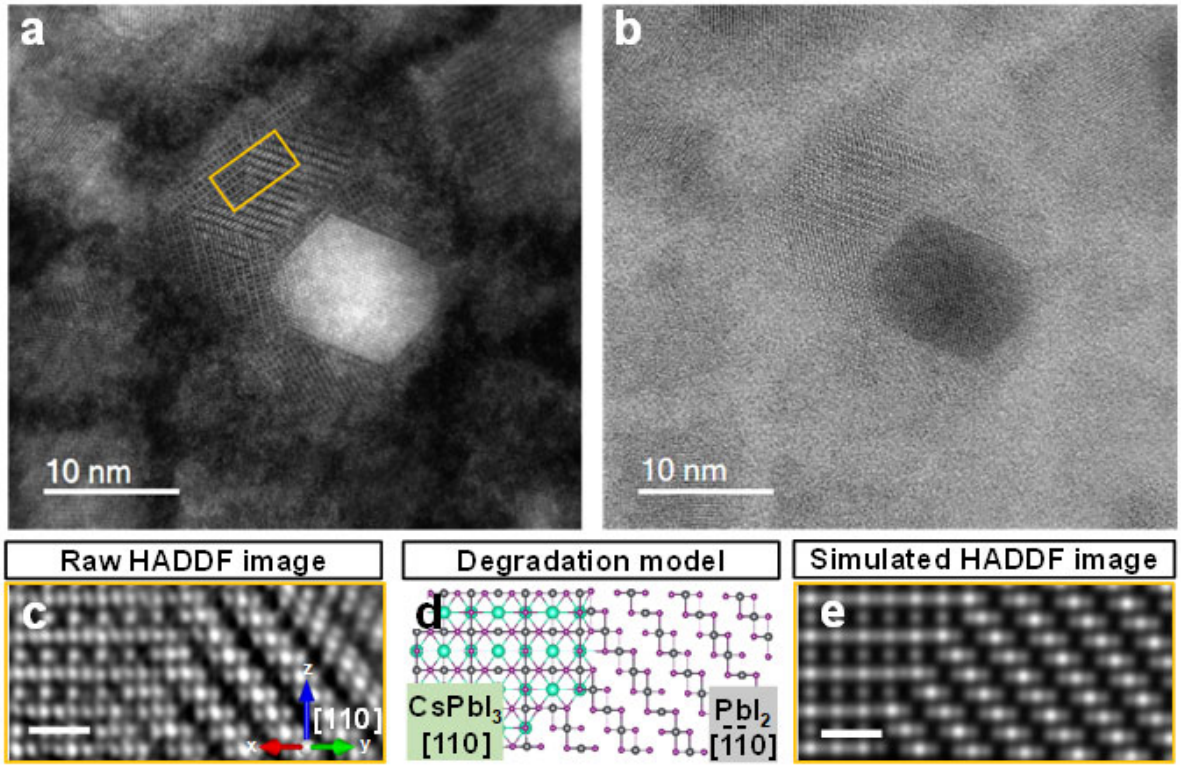

Supplementary Figure 9. **(a)** HAADF-STEM and **(b)** BF-STEM images for $Cs_{0.5}FA_{0.5}PbI_3$ sample; the image is viewed along the cubic [110] zone axis established from the lattice arrangement similar with the original $CsPbI_3$ (or $FAPbI_3$) cubic crystal structure. **(c)** the zoomed-in view, **(d)** the atomic models, and **(e)** the simulated atomic resolution HAADF-STEM image for the region marked with a yellow square in experimental HAADF-STEM image **(a)** of $Cs_{0.5}FA_{0.5}PbI_3$ along the [110] zone axis. All the experimental STEM images of the samples containing FA are distortion due to the fast decomposition of local crystal structure from $FAPbI_3$ to PbI_2 under e-beam illumination. Scale bar in **(c)** and **(e)**, 10 Å.

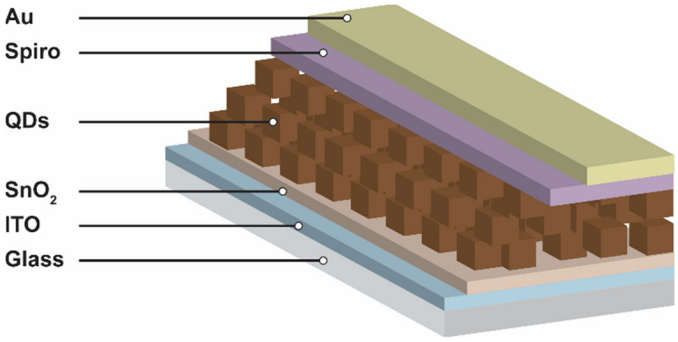

Supplementary Figure 10. Schematic device structure of QDSCs.

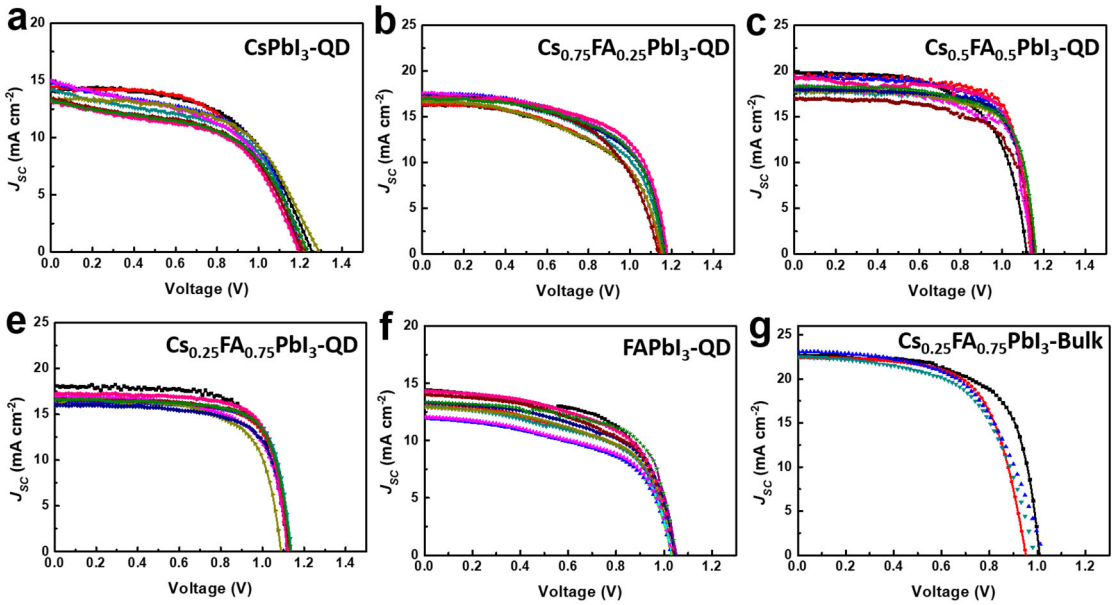

Supplementary Figure 11. Photocurrent density-voltage (*J-V*) characteristics of QDSCs (ten devices for each composition) with different compositions: (**a**) $CsPbI_3$ QD, (**b**) $Cs_{0.75}FA_{0.25}PbI_3$ QD, (**c**) $Cs_{0.5}FA_{0.5}PbI_3$ QD, (**d**) $Cs_{0.25}FA_{0.75}PbI_3$ QD, (**e**) $FAPbI_3$ QD; and (**g**) bulk $Cs_{0.25}FA_{0.75}PbI_3$ devices (four devices).

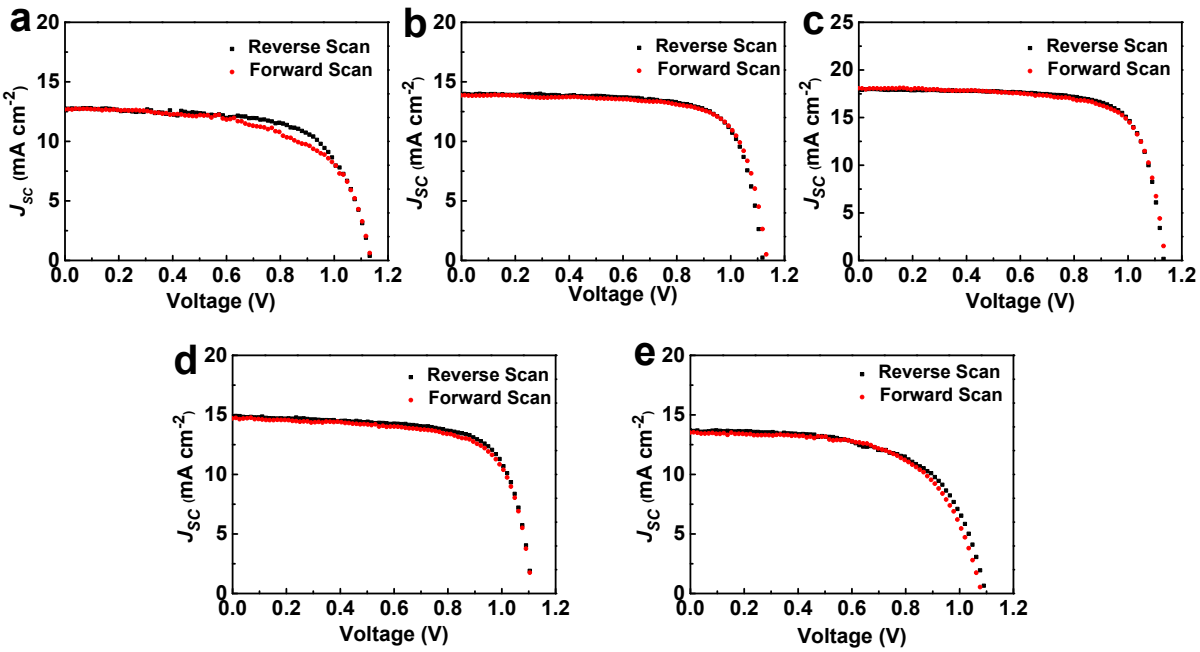

Supplementary Figure 12. *J-V* curves of a typical QD devices with different sweeping directions for (a) $CsPbI_3$ QD, (b) $Cs_{0.75}FA_{0.25}PbI_3$ QD, (c) $Cs_{0.5}FA_{0.5}PbI_3$ QD, (d) $Cs_{0.25}FA_{0.75}PbI_3$ QD, and (e) $FAPbI_3$ QD.

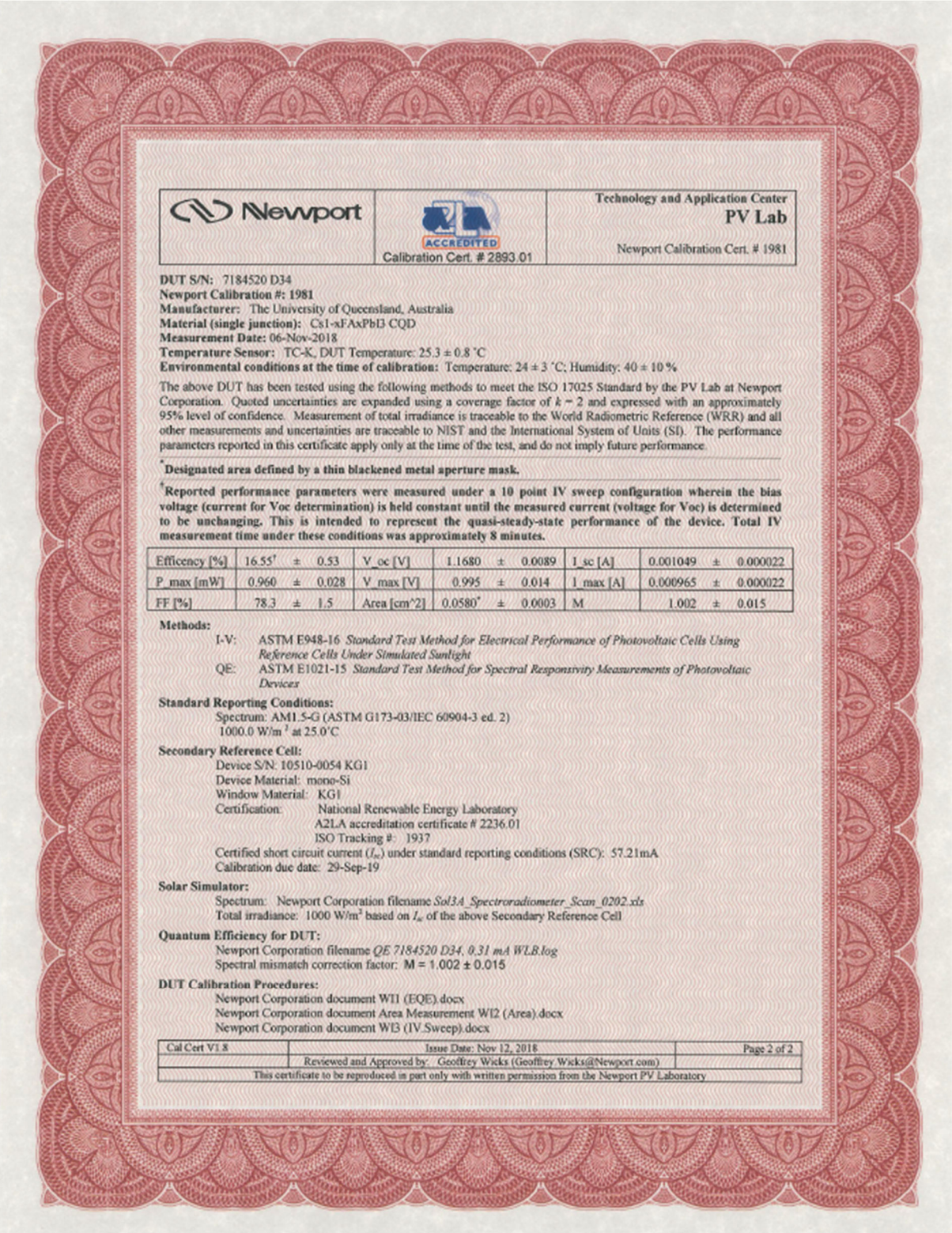

Newport

ACCREDITED
Calibration Cert. # 2893.01

Technology and Application Center
PV Lab
Newport Calibration Cert. # 1981

DUT S/N: 7184520 D34
Newport Calibration #: 1981
Manufacturer: The University of Queensland, Australia
Material (single junction): Cs1-xFAxPbI3 CQD
Measurement Date: 06-Nov-2018
Temperature Sensor: TC-K, DUT Temperature: 25.3 ± 0.8 °C
Environmental conditions at the time of calibration: Temperature: 24 ± 3 °C; Humidity: 40 ± 10 %

The above DUT has been tested using the following methods to meet the ISO 17025 Standard by the PV Lab at Newport Corporation. Quoted uncertainties are expanded using a coverage factor of $k \sim 2$ and expressed with an approximately 95% level of confidence. Measurement of total irradiance is traceable to the World Radiometric Reference (WRR) and all other measurements and uncertainties are traceable to NIST and the International System of Units (SI). The performance parameters reported in this certificate apply only at the time of the test, and do not imply future performance.

*Designated area defined by a thin blackened metal aperture mask.

†Reported performance parameters were measured under a 10 point IV sweep configuration wherein the bias voltage (current for Voc determination) is held constant until the measured current (voltage for Voc) is determined to be unchanging. This is intended to represent the quasi-steady-state performance of the device. Total IV measurement time under these conditions was approximately 8 minutes.

Efficency [%]	16.55†	±	0.53	V_oc [V]	1.1680	±	0.0089	I_sc [A]	0.001049	±	0.000022
P_max [mW]	0.960	±	0.028	V_max [V]	0.995	±	0.014	I_max [A]	0.000965	±	0.000022
FF [%]	78.3	±	1.5	Area [cm^2]	0.0580*	±	0.0003	M	1.002	±	0.015

Methods:
I-V: ASTM E948-16 *Standard Test Method for Electrical Performance of Photovoltaic Cells Using Reference Cells Under Simulated Sunlight*
QE: ASTM E1021-15 *Standard Test Method for Spectral Responsivity Measurements of Photovoltaic Devices*

Standard Reporting Conditions:
Spectrum: AM1.5-G (ASTM G173-03/IEC 60904-3 ed. 2)
1000.0 W/m² at 25.0°C

Secondary Reference Cell:
Device S/N: 10510-0054 KG1
Device Material: mono-Si
Window Material: KG1
Certification: National Renewable Energy Laboratory
A2LA accreditation certificate # 2236.01
ISO Tracking #: 1937
Certified short circuit current (I_{sc}) under standard reporting conditions (SRC): 57.21mA
Calibration due date: 29-Sep-19

Solar Simulator:
Spectrum: Newport Corporation filename *Sol3A_Spectroradiometer_Scan_0202.xls*
Total irradiance: 1000 W/m² based on I_{sc} of the above Secondary Reference Cell

Quantum Efficiency for DUT:
Newport Corporation filename *QE 7184520 D34, 0.31 mA WLB.log*
Spectral mismatch correction factor: M = 1.002 ± 0.015

DUT Calibration Procedures:
Newport Corporation document WI1 (EQE).docx
Newport Corporation document Area Measurement WI2 (Area).docx
Newport Corporation document WI3 (IV_Sweep).docx

Cal Cert V1.8	Issue Date: Nov 12, 2018	Page 2 of 2
	Reviewed and Approved by: Geoffrey Wicks (Geoffrey.Wicks@Newport.com)	
This certificate to be reproduced in part only with written permission from the Newport PV Laboratory		

Supplementary Figure 13. Certificated results from an internationally accredited PV laboratory (Newport, USA). The certificated efficiency is 16.55%. Our device active area was 0.08 cm^2, while certification, a mask with the area of 0.058 cm^2 was attached to the device.

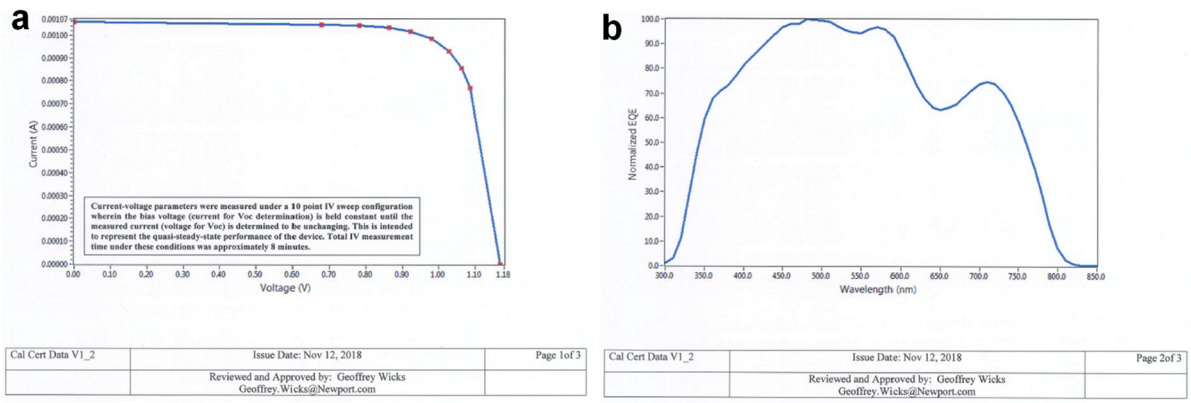

Supplementary Figure 14. (a) Certificated *J-V* curve and (b) Normalized EQE measured at Newport PV lab.

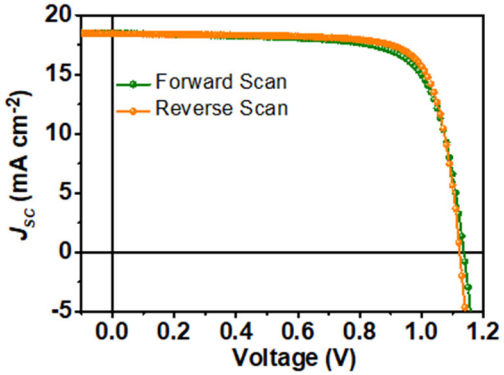

Supplementary Figure 15. *J-V* curves of the hero device with different sweeping directions tested at Newport PV lab, USA.

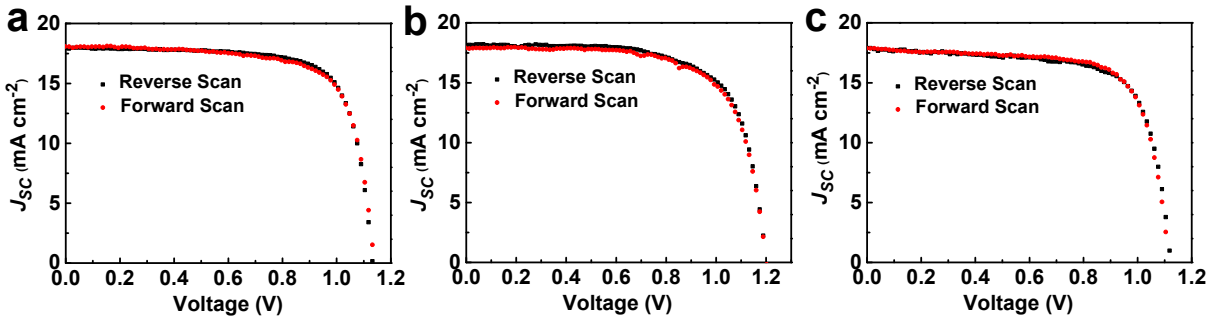

Supplementary Figure 16. *J-V* curves of additional three $Cs_{0.5}FA_{0.5}PbI_3$ QD devices with different sweeping directions tested in our lab at the University of Queensland.

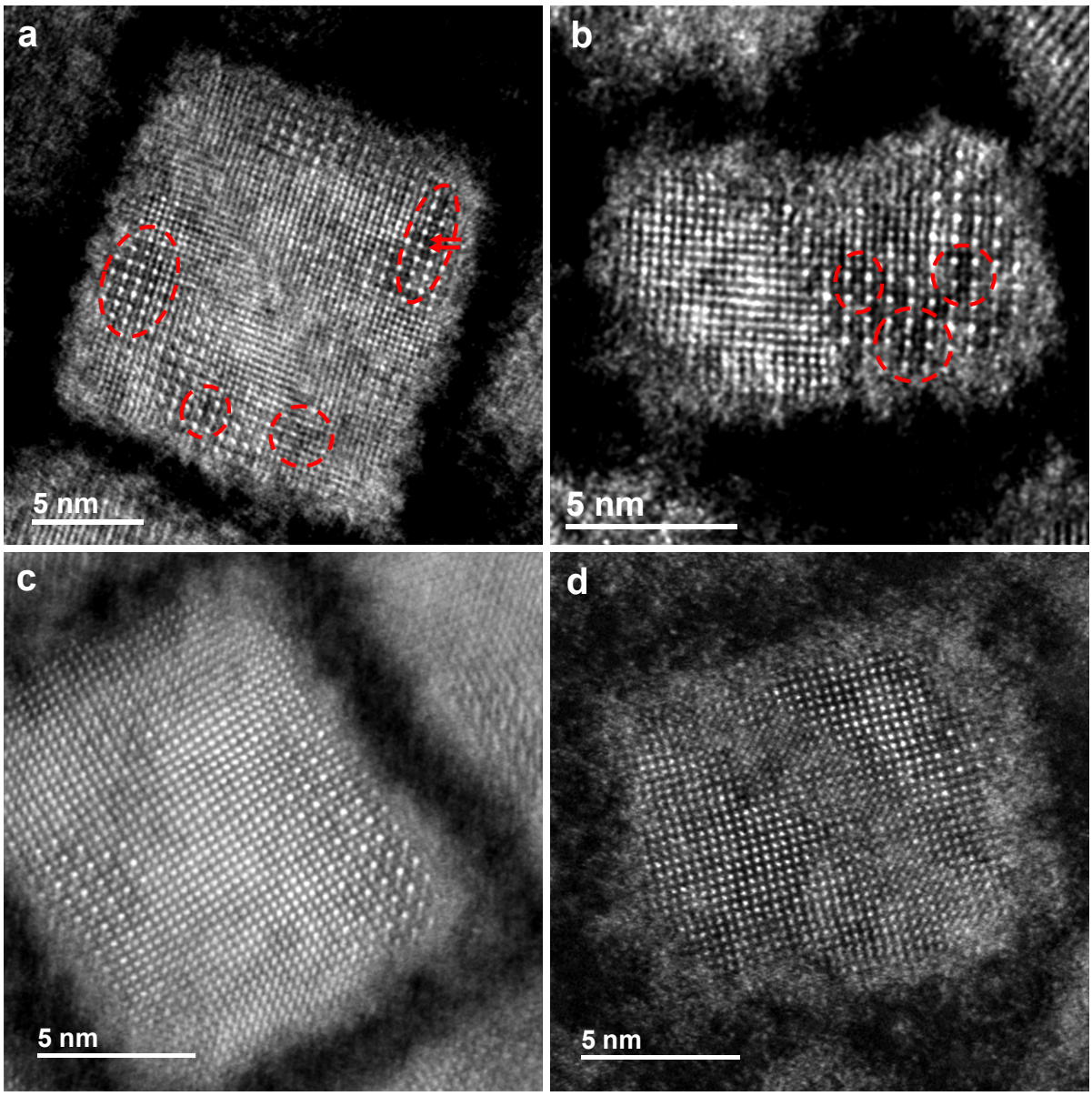

Supplementary Figure 17. Atomic-resolution HAADF-STEM images of $Cs_{0.5}FA_{0.5}PbI_3$ QDs obtained in OA-less condition (**a, b**) and $Cs_{0.5}FA_{0.5}PbI_3$ QDs obtained in the OA-rich condition (**c, d**). The circled areas indicate the defective sites.

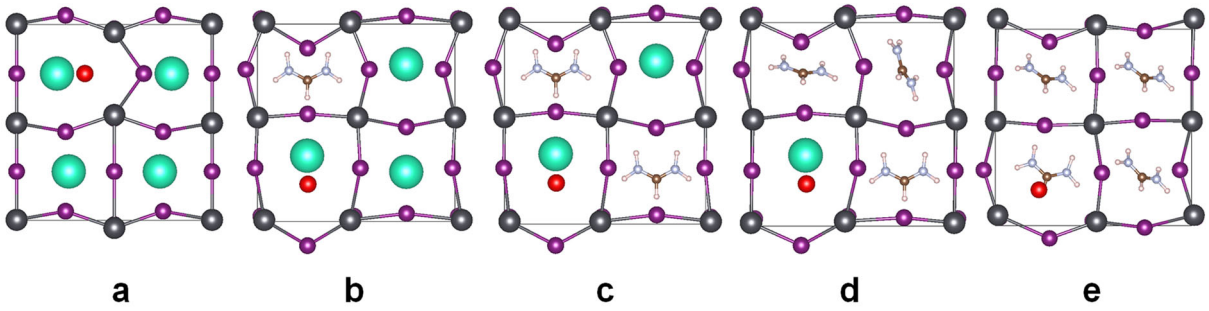

Supplementary Figure 18. Optimised atomic structures of bulk $Cs_{1-x}FA_xPbI_3$ crystals with I_i defect. (**a**) $CsPbI_3$; (**b**) $Cs_{0.75}FA_{0.25}PbI_3$; (**c**) $Cs_{0.5}FA_{0.5}PbI_3$; (**d**) $Cs_{0.25}FA_{0.75}PbI_3$; (**e**) $FAPbI_3$. Key: Green, Cs; dark gray, Pb; purple, I; brown, C; blue, N; pink, H; yellow, I_i.

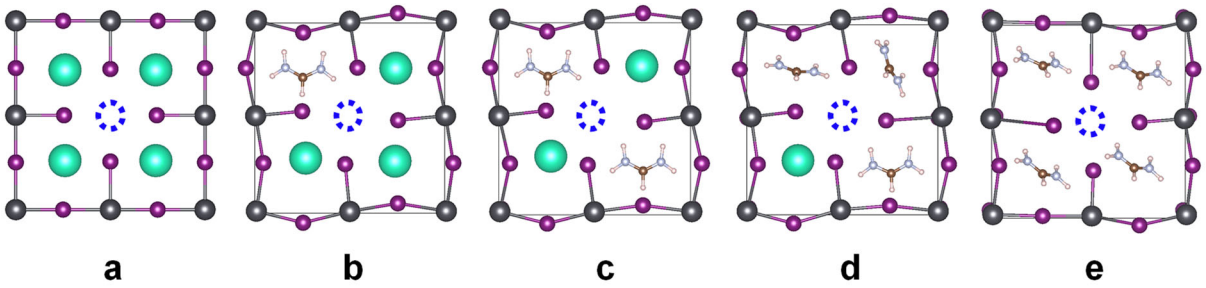

Supplementary Figure 19. Optimised atomic structures of bulk $Cs_{1-x}FA_xPbI_3$ crystals with V_{Pb} defect. (**a**) $CsPbI_3$; (**b**) $Cs_{0.75}FA_{0.25}PbI_3$; (**c**) $Cs_{0.5}FA_{0.5}PbI_3$; (**d**) $Cs_{0.25}FA_{0.75}PbI_3$;(**e**) $FAPbI_3$. Key: Green, Cs; dark gray, Pb; purple, I; brown, C; blue, N; pink, H; red dotted circle, V_{Pb}.

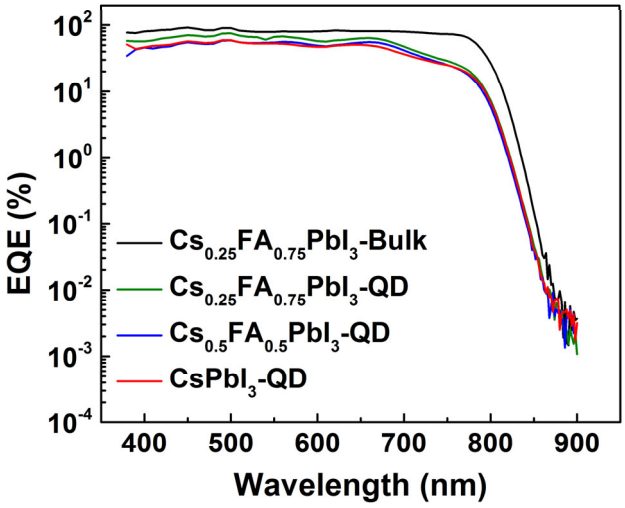

Supplementary Figure 20. Sensitive external quantum efficiencies (EQEs) of the QDs and bulk devices spanning nearly 5 orders of magnitude in photocurrent.

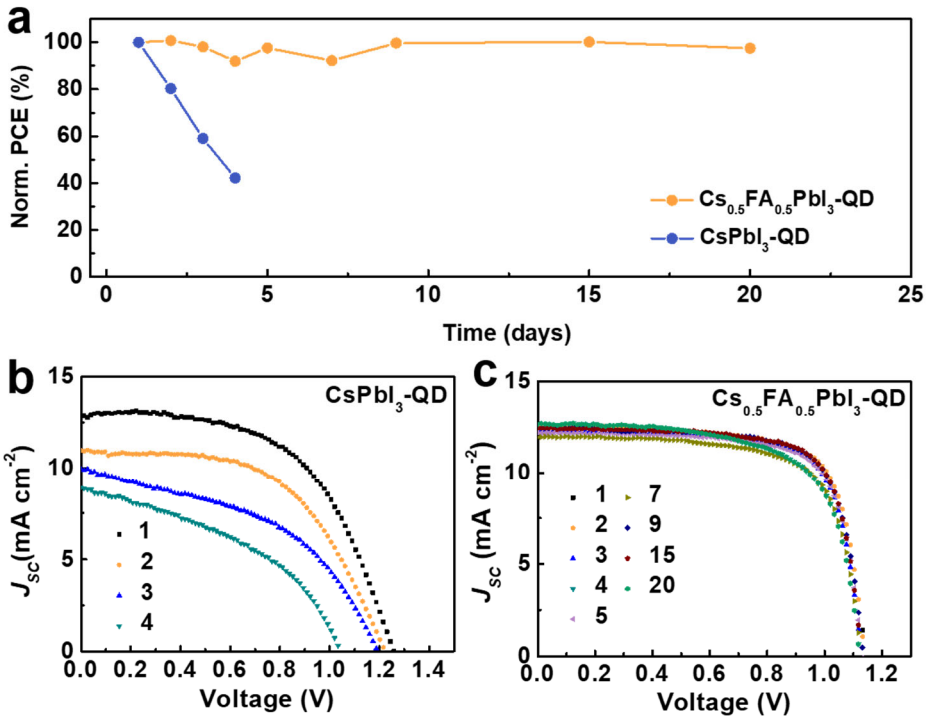

Supplementary Figure 21. (**a**) Normalized PCEs of the typical devices fabricated with $CsPbI_3$ QDs and $Cs_{0.5}FA_{0.5}PbI_3$ QDs (derived in an OA-rich environment) tested in ambient air without encapsulation as a function of storage time. The relative humidity was *ca.* 50-70% and the room temperature was *ca.* 25 ℃ for aging tests. *J-V* curves of the corresponding $CsPbI_3$ (**b**) and $Cs_{0.5}FA_{0.5}PbI_3$ (**c**) QDSCs.

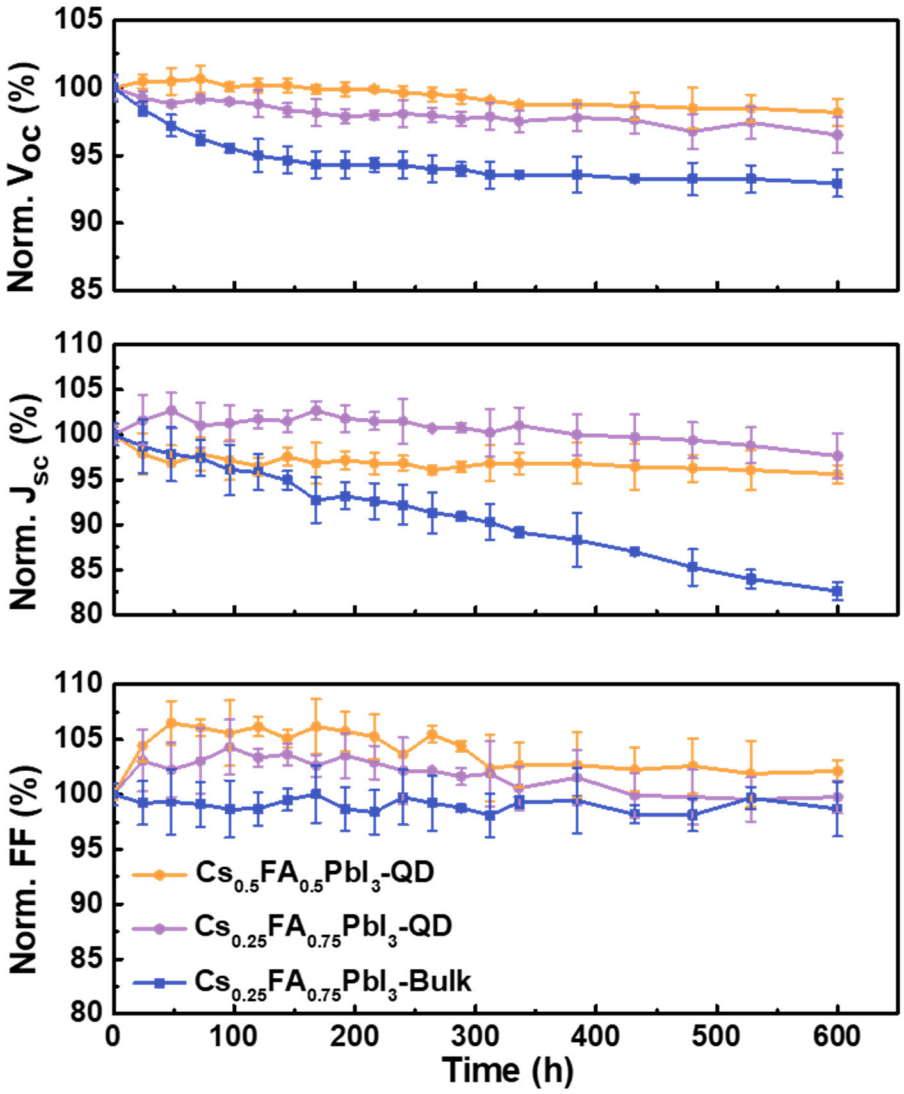

Supplementary Figure 22. Parameters of (**a**) V_{OC}, (**b**) J_{SC} and (**c**) FF evolution of solar cells fabricated with $Cs_{0.25}FA_{0.75}PbI_3$-Bulk, $Cs_{0.25}FA_{0.75}PbI_3$-QD, and $Cs_{0.5}FA_{0.5}PbI_3$-QD films monitored at open-circuit under 1-sun illumination in N_2 atmosphere. Mixed-cation QDs were derived in an OA-rich environment. Note that when QDSCs are under prolonged light illumination, the photogenerated charge carriers could neutralize the defects at QD surfaces and device interfaces, which will enhance the electronic coupling within the QD films and thus improve the transport of the dissociated charge carriers to respective electrodes[7]. In addition, the charge accumulation at the electrode interfaces would be decreased due to the built-in electric field under light illumination. These may explain why the FF of the QD devices shows slight increase with light illumination.

Supplementary Table 1. Ligand density in perovskite QD solutions.

Purification times	$CsPbI_3$	$FAPbI_3$
0	25-40	20-35
1	2.5-5.5	9-15
2	0.1-0.2	1-5
	$Cs_{1-x}FA_xPbI_3$	
0	2.5-10	
1	1.0-5.5	
2	0.1-0.5	

The unit is molar ratio of ligand/Pb in QD solution at all stages.

Supplementary Table 2. Bandgaps of $Cs_{1-x}FA_xPbI_3$ QDs determined from their UV-vis absorption spectra and Tauc analysis.

QDs	Bandgap (eV)
$CsPbI_3$	1.76
$Cs_{0.75}FA_{0.25}PbI_3$	1.71
$Cs_{0.5}FA_{0.5}PbI_3$	1.64
$Cs_{0.25}FA_{0.75}PbI_3$	1.58
$FAPbI_3$	1.55

Supplementary Table 3. Photovoltaic parameters of typical QDSCs using different QDs including $CsPbI_3$-QD, $Cs_{0.5}FA_{0.5}PbI_3$-QD-OL, and $Cs_{0.5}FA_{0.5}PbI_3$-QD-OA.

Samples	PCE (%)	J_{sc} (mA cm^{-2})	V_{oc} (V)	FF (%)
$CsPbI_3$-QD	9.0±0.58 (9.6)	15.1±0.37 (15.4)	1.14±0.02 (1.16)	52.3±1.39 (53.9)
$Cs_{0.5}FA_{0.5}PbI_3$-QD-OL	9.7±0.46 (10.1)	14.2±0.40 (14.6)	1.08±0.02 (1.08)	63.1±0.93 (64.1)
$Cs_{0.5}FA_{0.5}PbI_3$-QD-OA	15.3±0.85 (16.1)	17.9±0.46 (18.4)	1.13±0.02 (1.13)	75.4±2.18 (77.9)

Supplementary Table 4. Key parameters extracted from detailed balance analysis.

	V_{OC} [V]	PLQY	$\Delta V_{OC,NR}$ [V]	V_{OC} radiative limit [V]	$\Delta V_{OC,SR}$ [V]	μ_{bulk} [V]	$\Delta V_{OC,R}$ [V]	$j_{0,R}$ [A/cm^2]
$Cs_{0.25}FA_{0.75}PbI_3$-Bulk	1	0.003	0.15	1.25	0.1	1.1	0.26	1.10E-23
$Cs_{0.25}FA_{0.75}PbI_3$-QD	1.14	0.1	0.06	1.27	0.07	1.21	0.24	3.20E-24
$Cs_{0.5}FA_{0.5}PbI_3$-QD	1.13	0.075	0.07	1.27	0.08	1.21	0.24	2.60E-24
$CsPbI_3$-QD	1.11	0.065	0.07	1.26	0.09	1.19	0.25	3.00E-24

References

1. Kresse G, Furthmüller J. Efficiency of ab-initio total energy calculations for metals and semiconductors using a plane-wave basis set. *Computational Materials Science* **6**, 15-50 (1996).

2. Kresse G, Joubert D. From ultrasoft pseudopotentials to the projector augmented-wave method. *PHYSICAL REVIEW B* **59**, 1758-1775 (1999).

3. Perdew JP, Burke K, Ernzerhof M. Generalized Gradient Approximation Made Simple. *Physical Review Letters* **77**, 3865-3868 (1996).

4. Protesescu L*, et al.* Dismantling the "Red Wall" of Colloidal Perovskites: Highly Luminescent Formamidinium and Formamidinium–Cesium Lead Iodide Nanocrystals. *ACS Nano* **11**, 3119-3134 (2017).

5. Brouwer AM. Standards for photoluminescence quantum yield measurements in solution (IUPAC Technical Report). *Pure and Applied Chemistry* **83**, 2213-2228 (2011).

6. Chen S*, et al.* Atomic scale insights into structure instability and decomposition pathway of methylammonium lead iodide perovskite. *Nat. Commun.* **9**, 4807 (2018).

7. Zhao C, Chen B, Qiao X, Luan L, Lu K, Hu B. Revealing underlying processes involved in light soaking effects and hysteresis phenomena in perovskite solar cells. *Advanced Energy Materials* **5**, 1500279 (2015).